Supplementary Information

Phase-transition induced giant negative electrocaloric effect in a lead-free relaxor ferroelectric thin film

Biaolin Peng[1,2,3], Qi Zhang[3]*, Gang Bai[4], Glenn J.T. Leighton[3], Christopher Shaw[3], Steven J. Milne[5], Bingsuo Zou[1], Wenhong Sun[1], Haitao Huang[2,]*, Zhonglin Wang[6]*

[1]Center on Nanoenergy Research, School of Physical Science & Technology, Guangxi University, Nanning 530004, China

[2]Department of Applied Physics, The Hong Kong Polytechnic University, Kowloon, Hong Kong SAR

[3]Department of Manufacturing and Materials, Cranfield University, Cranfield, Bedfordshire, MK43 0AL, United Kingdom

[4]College of Electronic and Optical Engineering & College of Microelectronics, Nanjing University of Posts and Telecommunications, Nanjing 210023, China

[5]Institute for Materials Research, University of Leeds, Leeds LS2 9JT, UK

[6]School of Materials Science and Engineering, Georgia Institute of Technology, Atlanta, GA 30332-0245, USA

*Correspondence to: q.zhang@cranfield.com, aphhuang@polyu.edu.hk, zhong.wang@mse.gatech.edu

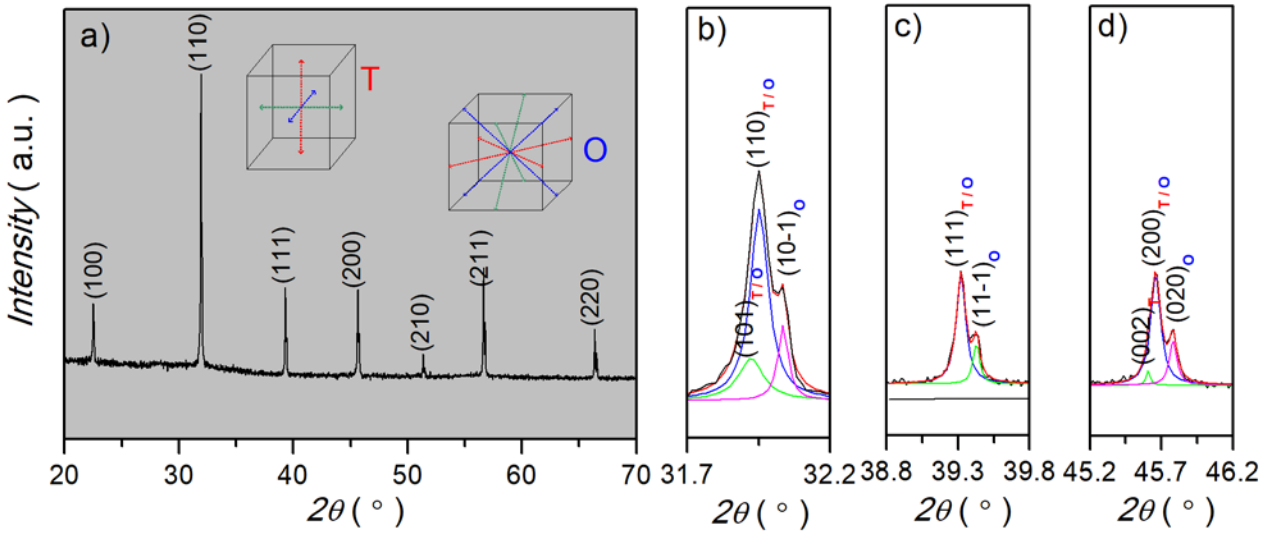

Figure S1. XRD pattern of the $0.5(Ba_{0.8}Ca_{0.2})TiO_3$-$0.5Bi(Mg_{0.5}Ti_{0.5})O_3$ (BCT-BMT) bulk ceramic. The abbreviations *T* and *O* represent tetragonal and orthorhombic phases, respectively.

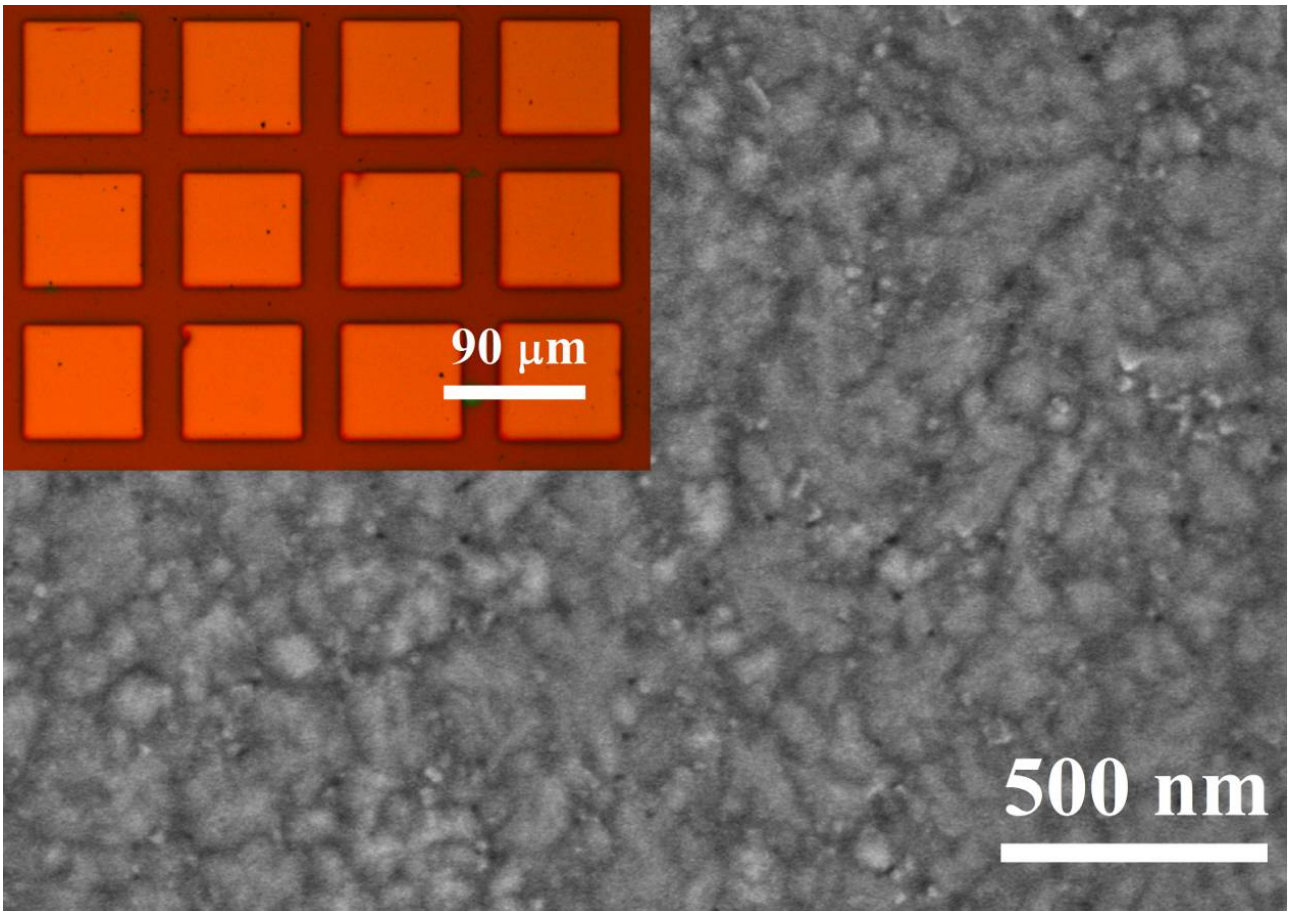

Figure S2. Surface SEM image of the BCT-BMT thin film. Inset: the optical microscope image of top electrodes.

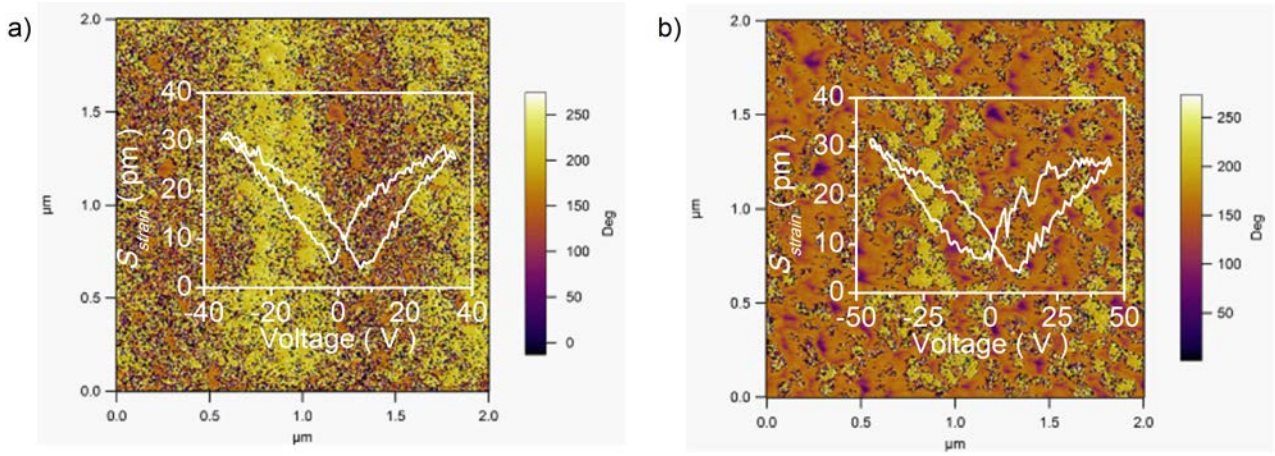

Figure S3. PFM vertical phase images of the BCT-BMT thin film after the first scanning cycle with 20 V dc bias applied. a) The second scanning cycle with dc bias withdrawn. b) The third scanning cycle with dc bias withdrawn. Insets in a) and b): the butterfly curves of the voltage strain response at 40 V and 50 V, respectively.

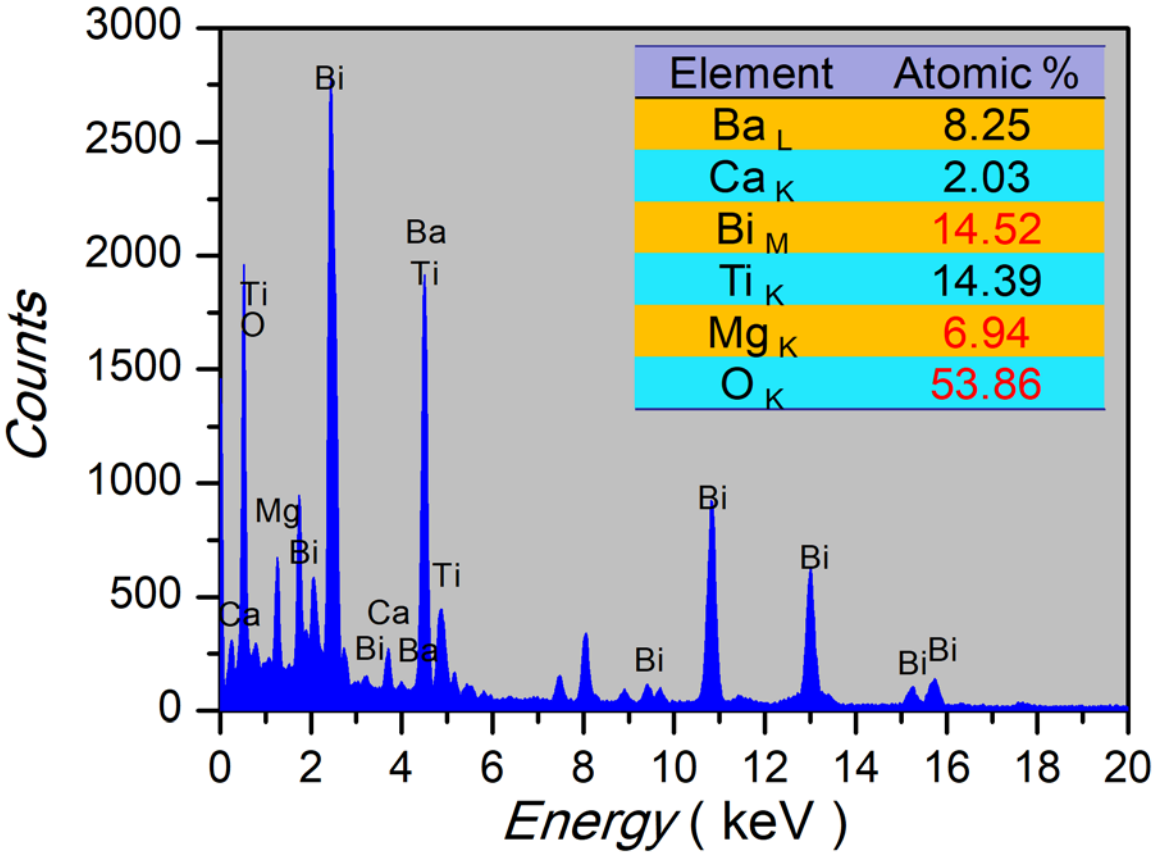

Figure S4. Cross-sectional EDS diagram in TEM sample. Inset lists: the atomic percentages of the elements.

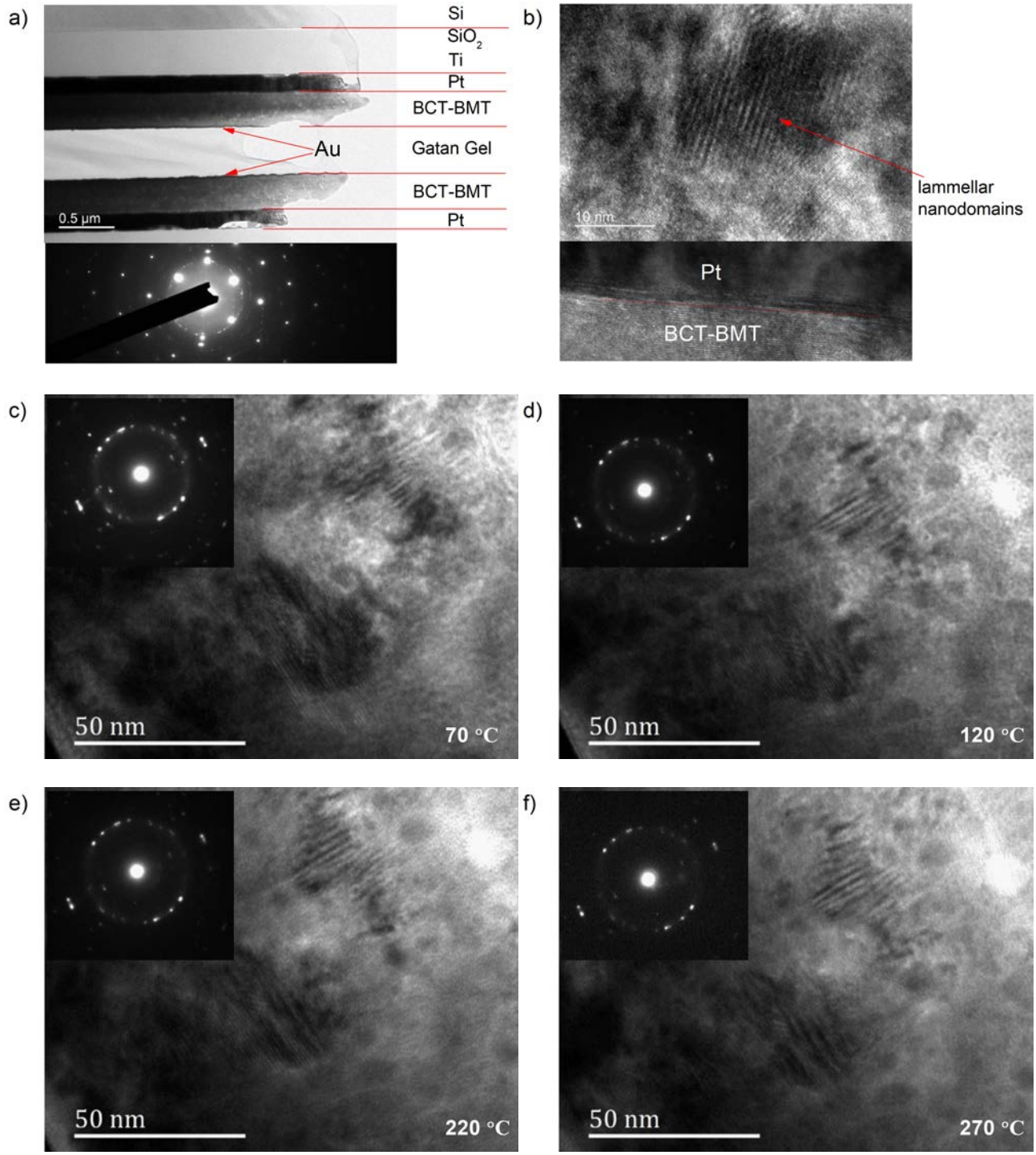
a)
Si
SiO2
Ti
Pt
BCT-BMT
Au
Gatan Gel
BCT-BMT
Pt
0.5 μm
b)
lammellar
nanodomains
10 nm
Pt
BCT-BMT
c)
50 nm
70 °C
d)
50 nm
120 °C
e)
50 nm
220 °C
f)
50 nm
270 °C

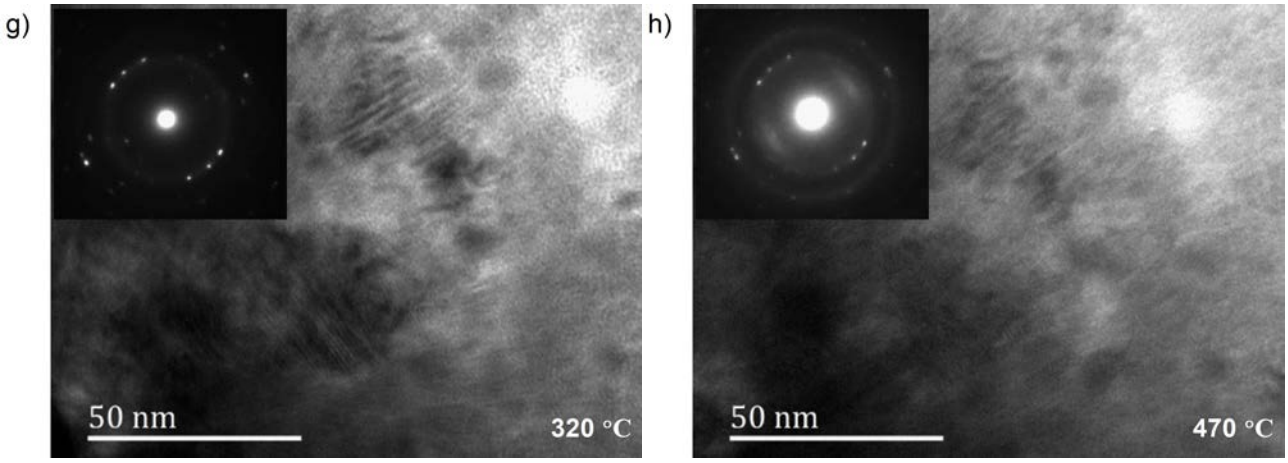

Figure S5. | Cross-sectional TEM images of the BCT-BMT thin film. (a) Cross-sectional TEM image (the upper part) and SAED pattern (the lower part). **(b)** HRTEM images of ferroelectric domains (the upper part) and the electrode-thin-film interface (the lower part). **(c) - (h)** Evolution of ferroelectric nanodomains as the temperature increased from 20 °C to 470 °C.

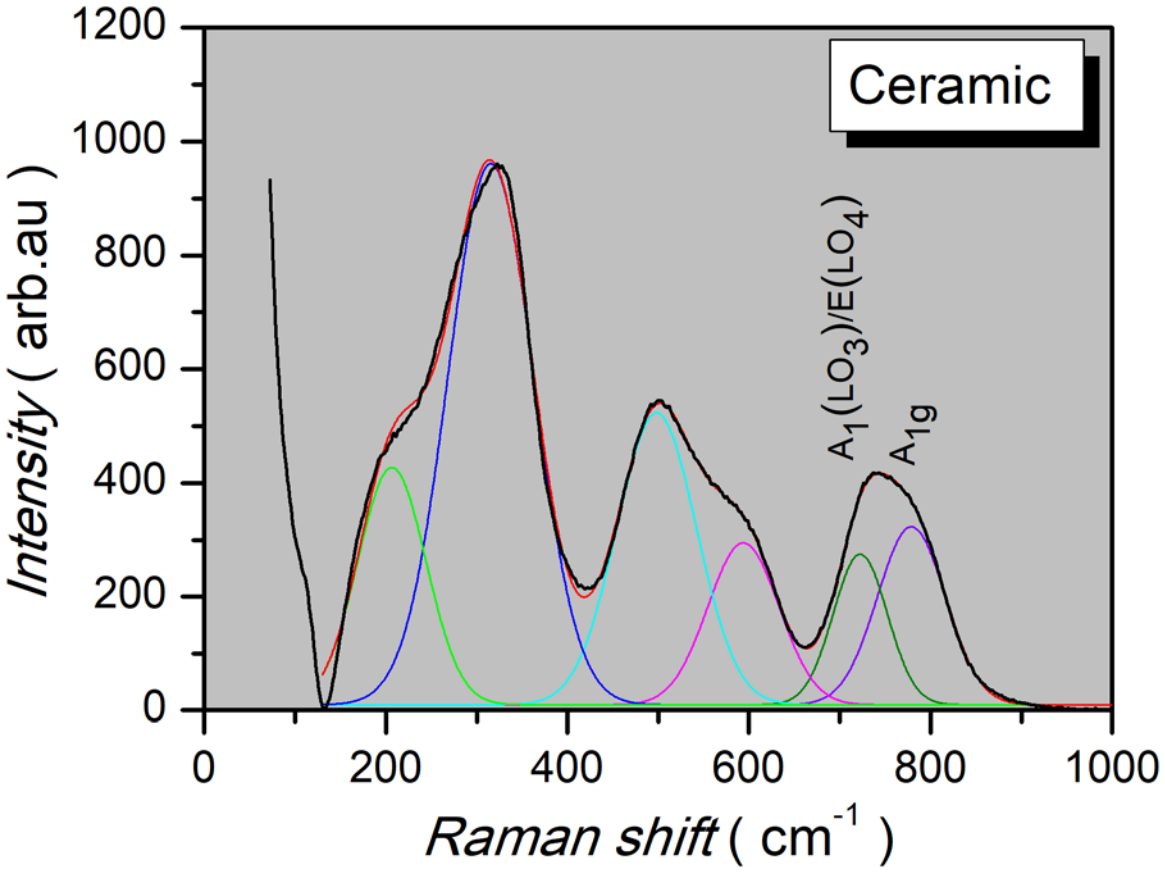

Figure S6. Raman scattering spectra of the BCT-BMT bulk ceramic.

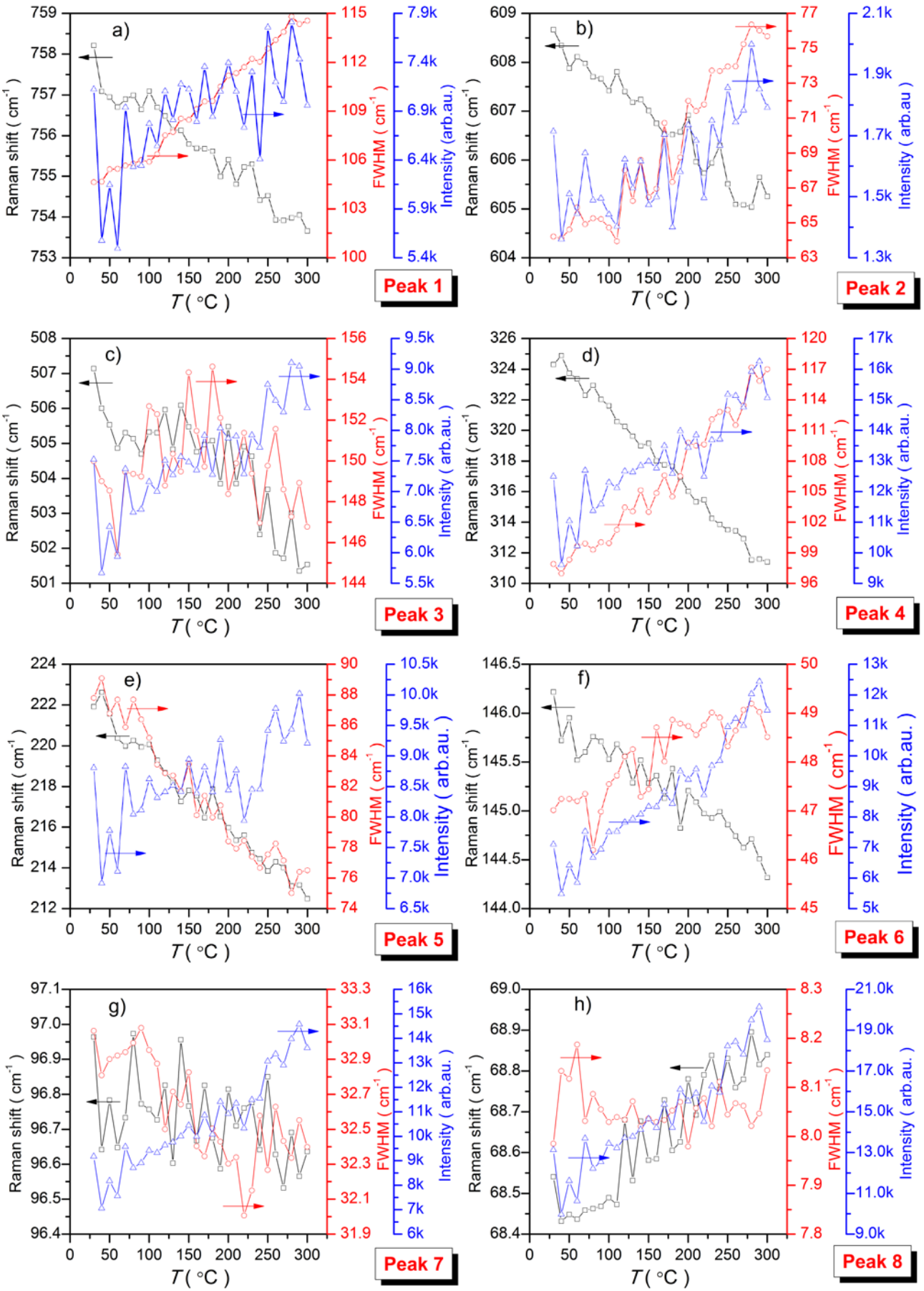
a)
Raman shift (cm^{-1})
FWHM (cm^{-1})
Intensity (arb.au.)
T (°C)
Peak 1
b)
Raman shift (cm^{-1})
FWHM (cm^{-1})
Intensity (arb.au)
T (°C)
Peak 2
c)
Raman shift (cm^{-1})
FWHM (cm^{-1})
Intensity (arb.au.)
T (°C)
Peak 3
d)
Raman shift (cm^{-1})
FWHM (cm^{-1})
Intensity (arb.au.)
T (°C)
Peak 4
e)
Raman shift (cm^{-1})
FWHM (cm^{-1})
Intensity (arb.au.)
T (°C)
Peak 5
f)
Raman shift (cm^{-1})
FWHM (cm^{-1})
Intensity (arb.au.)
T (°C)
Peak 6
g)
Raman shift (cm^{-1})
FWHM (cm^{-1})
Intensity (arb.au.)
T (°C)
Peak 7
h)
Raman shift (cm^{-1})
FWHM (cm^{-1})
Intensity (arb.au.)
T (°C)
Peak 8

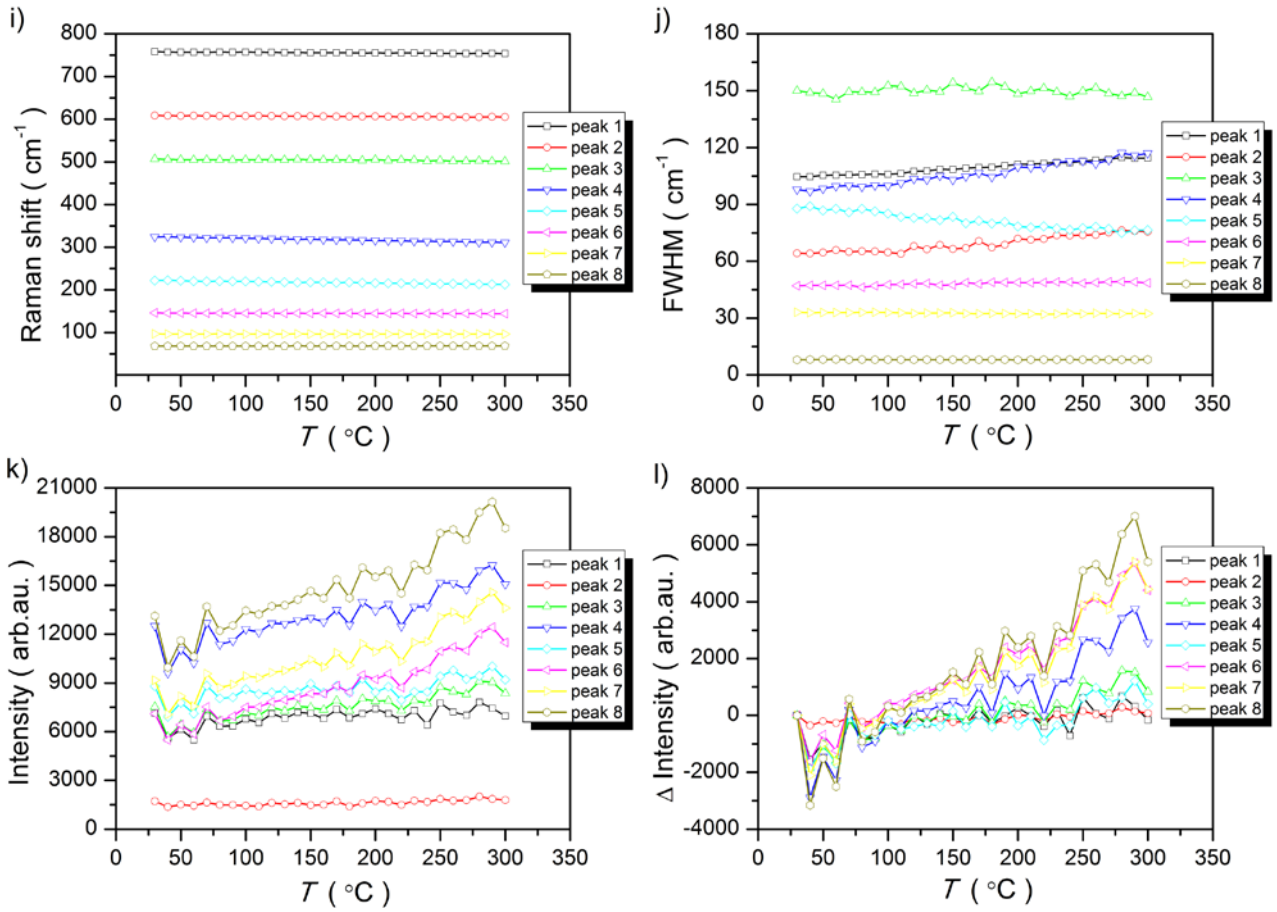

Figure S7. Raman scattering spectra measurements as a function of temperature of the BCT-BMT thin films. (a)-(h) Raman shift, FWHM and intensity for peaks 1-8, respectively. **i)** Raman shift, **j)** FWHM, **k)** Raman intensity and **l)** Δ Raman intensity as a function of temperature for all the peaks.

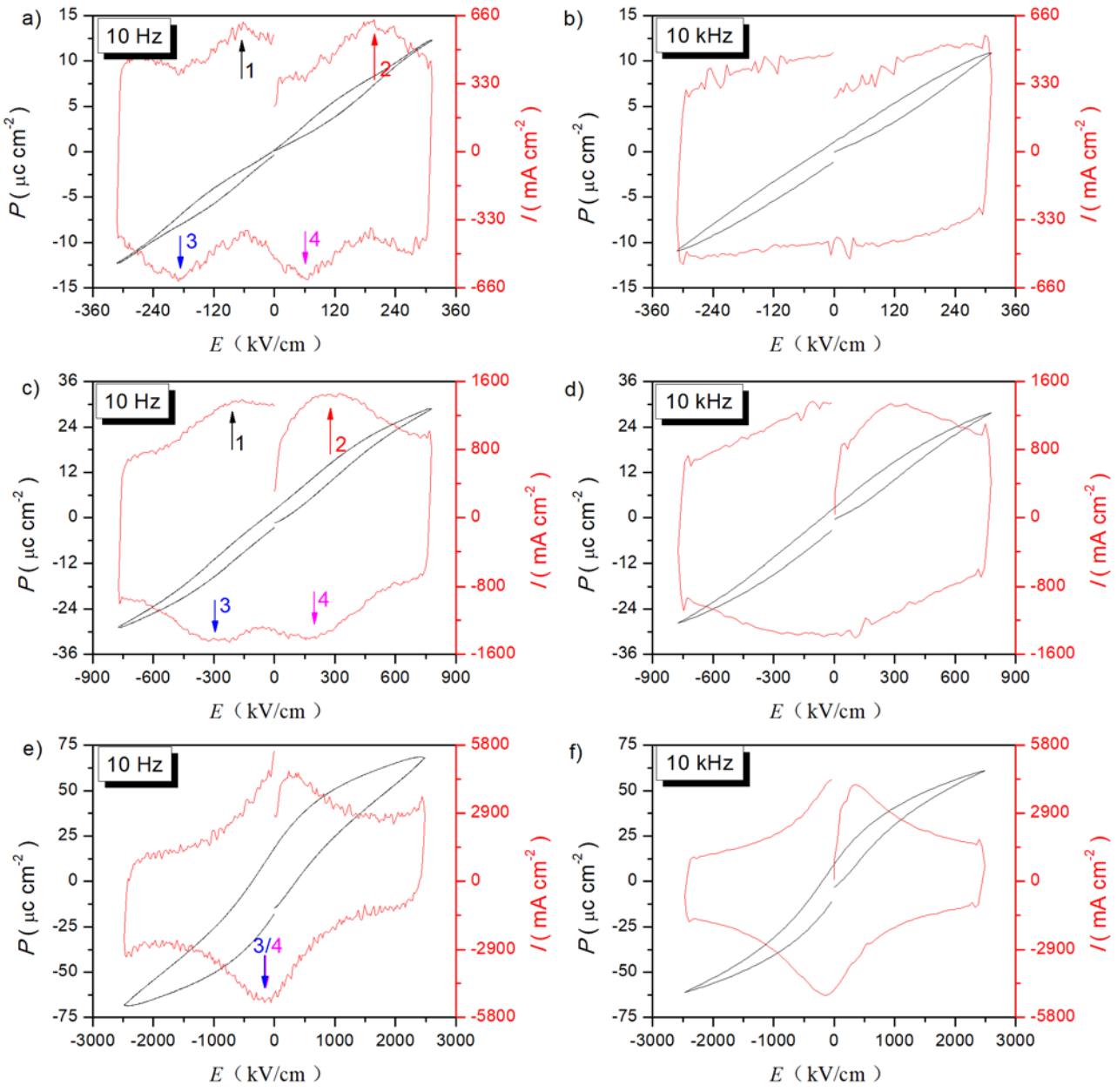

Figure S8. *P-E* loops and corresponding *I-E* curves of the BCT-BMT thin films at selected electric fields. a), c) and e) measured at 10 Hz. b), d) and f) measured at 10 kHz.

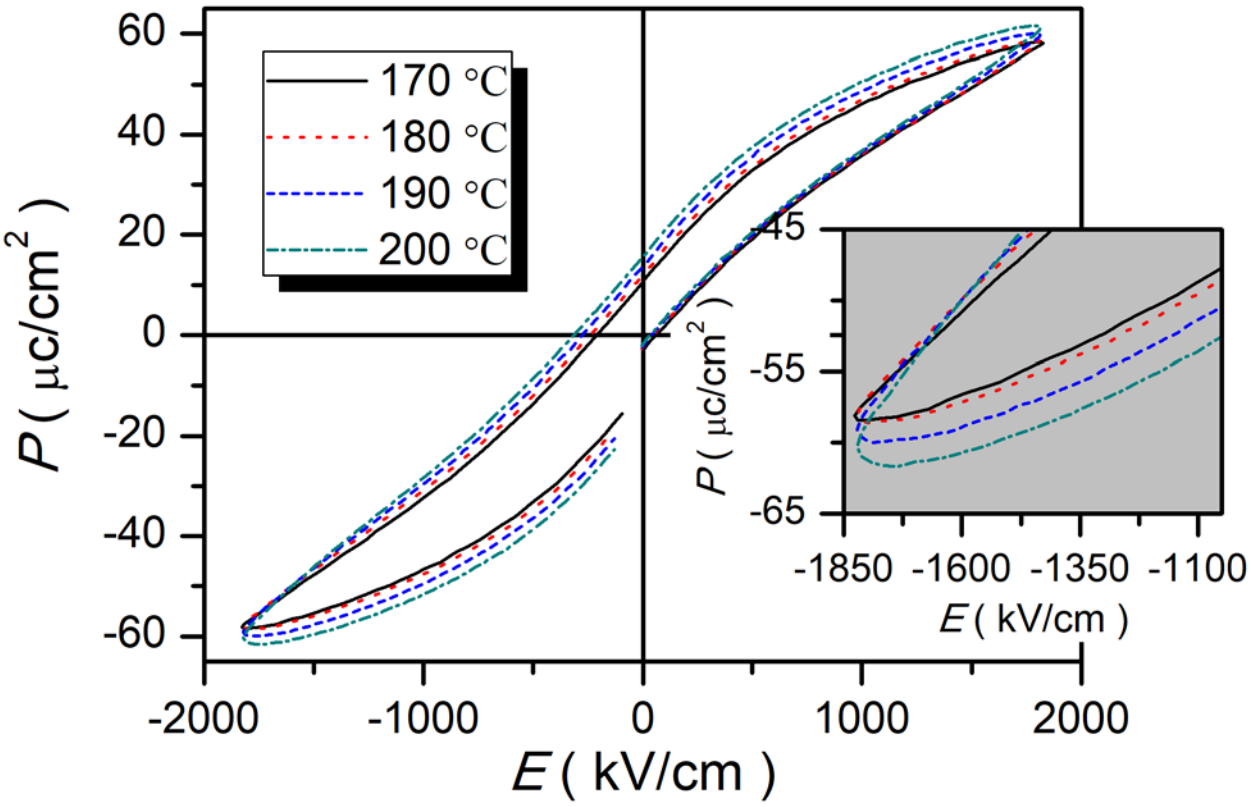

Figure S9. P-E loops measured at higher temperatures. Inset: magnified view.

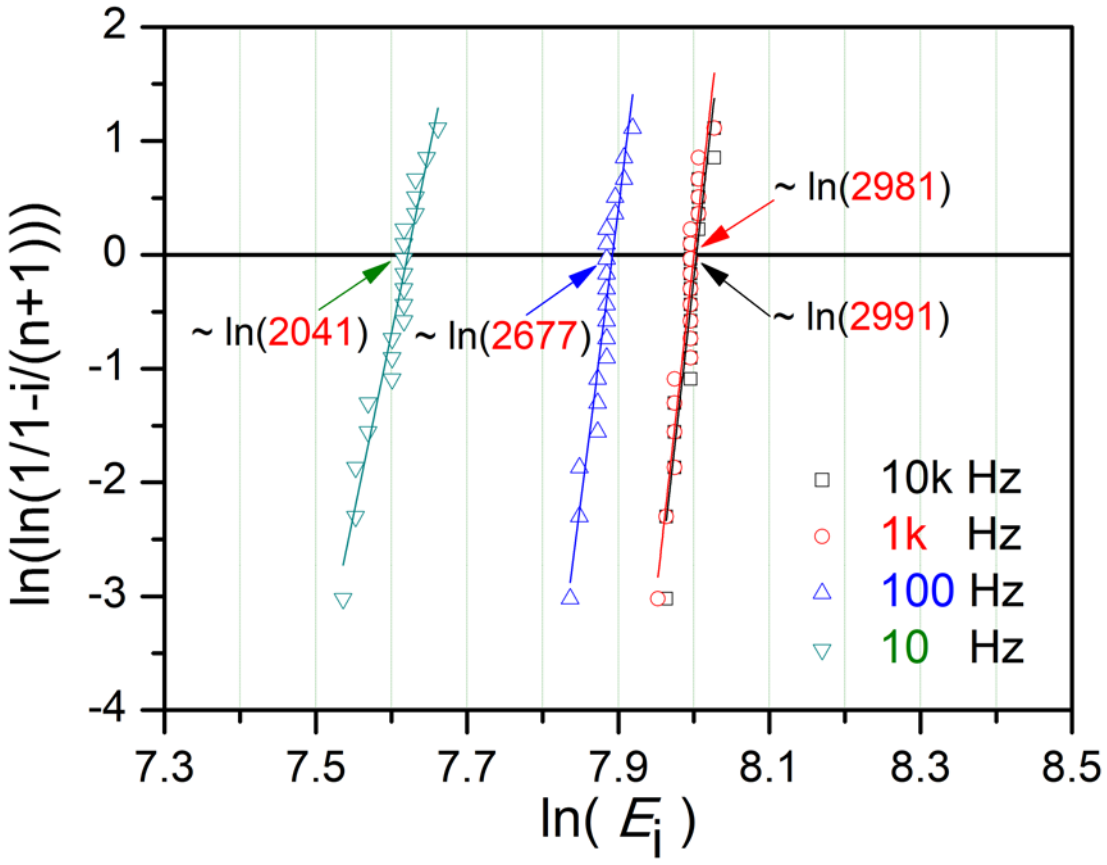

Figure S10. Weibull distribution of the dielectric breakdown strength at different frequencies. Where n is the total number of samples, E_i is the breakdown electric field of the *i*th specimen arranged in ascending order ($E_1 \leq E_2 \leq E_3 \ldots \leq E_n$). The mean dielectric breakdown strength (DBS) can be extracted from the point where the fitting line intersects with the horizontal axis at ln(ln(1/(1-i/(n+1)))) = 0. [1]

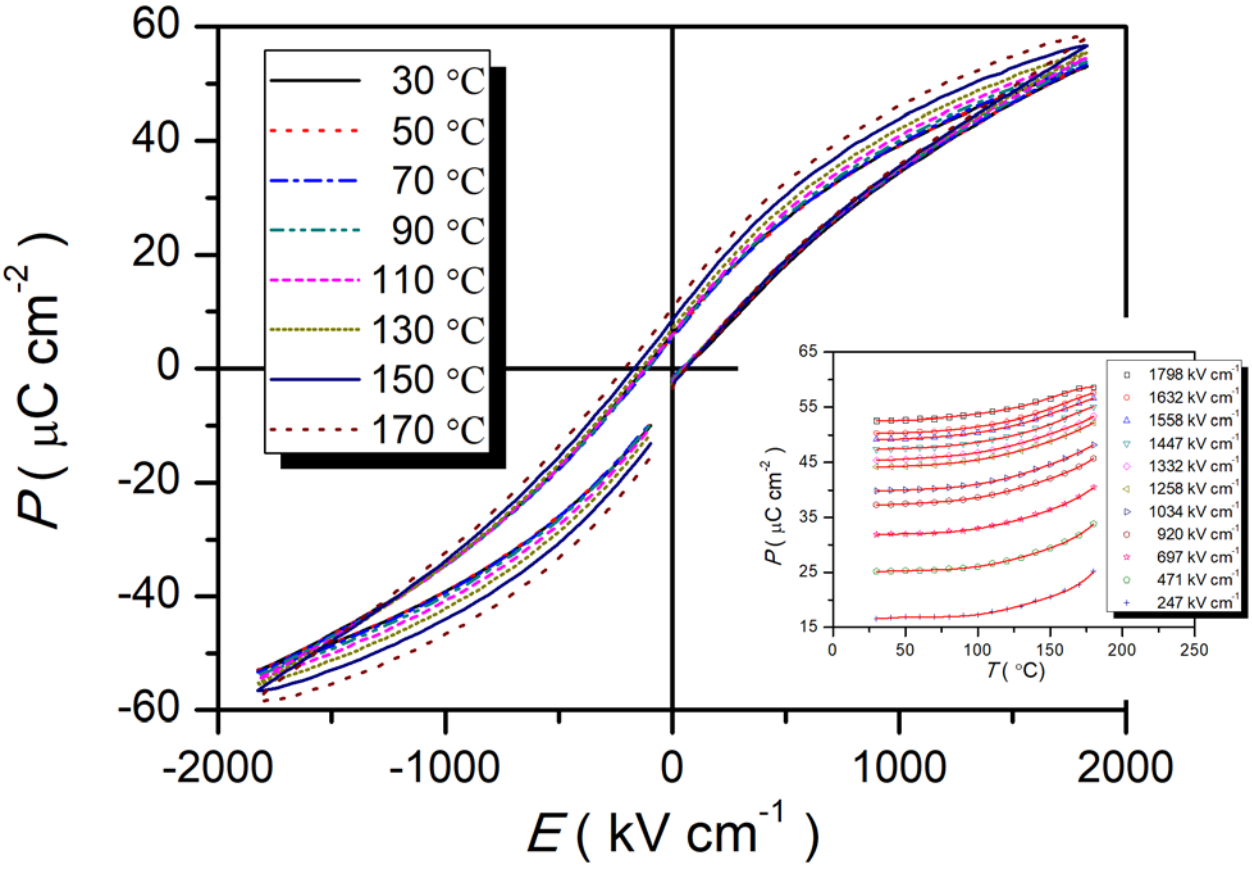

Figure S11. *P-E* loops at selected temperatures of the BCT-BMT thin film. Inset: *P(T)* at selected electric fields.

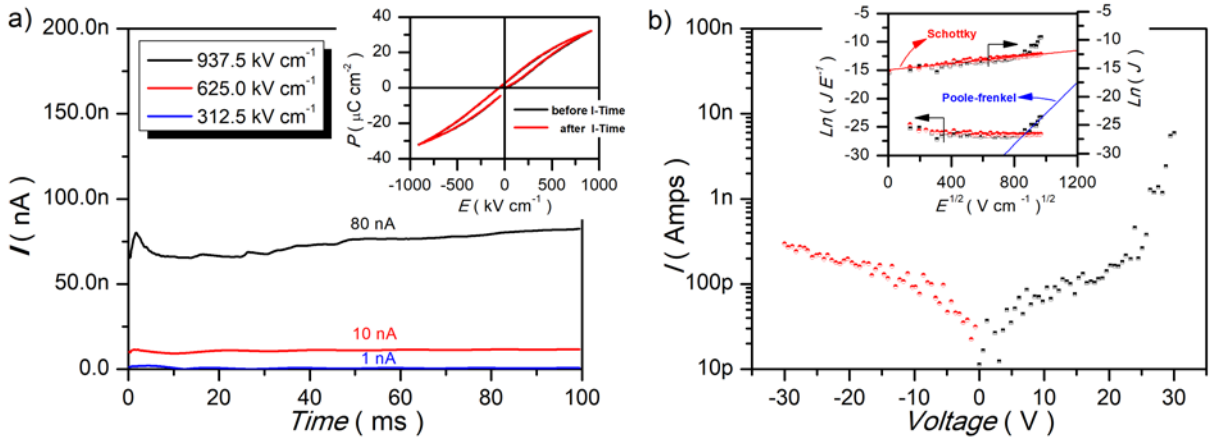

Figure S12. Leakage current measurements of the BCT-BMT thin film. (a) Leakage current at selected electric fields. Inset: *P*-*E* loops before and after the measurements of leakage current. **(b)** *I*(*V*). Inset: The ln(*J*/*E*) and ln(*J*) is plotted as a function of $E^{1/2}$. The red and blue straight lines are fitted following the Schottky and Poole-Frenkel conduction mechanisms, respectively. The leakage current densities due to Schottky emission conduction mechanisms and Poole-Frenkel emission conduction mechanisms can be expressed as $J \propto T^2 \exp\left[\frac{q\left(-\Phi_B + \sqrt{qE/4\pi\varepsilon}\right)}{kT}\right]$ and $J \propto E \exp\left[\frac{q\left(-\Phi_B + \sqrt{qE/\pi\varepsilon}\right)}{kT}\right]$, respectively; where J denotes current density, T represents the absolute temperature, k is the Boltzmann constant, q denotes the electronic charge, E represents the electric field, Φ_B is the barrier height, and ε denotes the dielectric constant of the thin film.

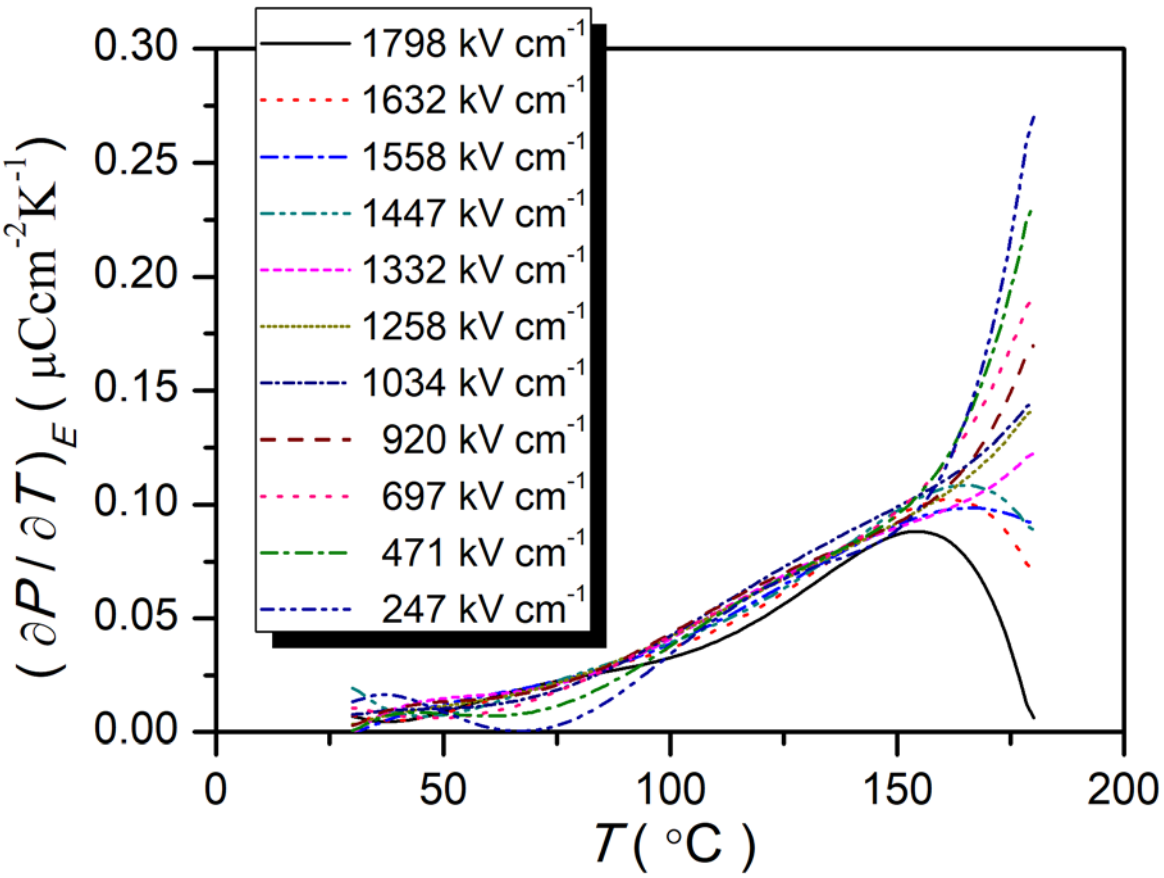

Figure S13. $(\partial P/\partial T)_E(T)$ at selected electric fields of the BCT-BMT thin film.

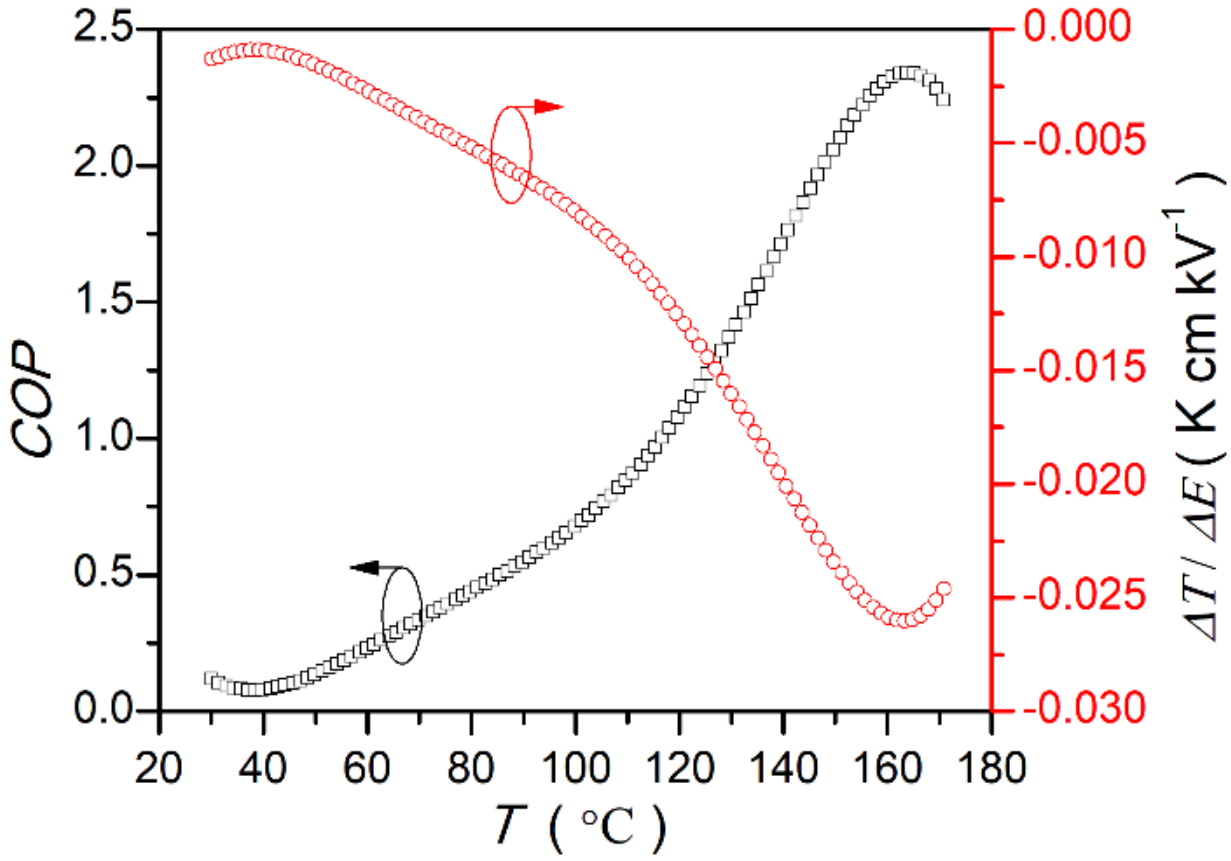

Figure S14. ***COP*** **and** $\Delta T_{max}/\Delta E_{max}$ **of the BCT-BMT relaxor ferroelectric thin film.**

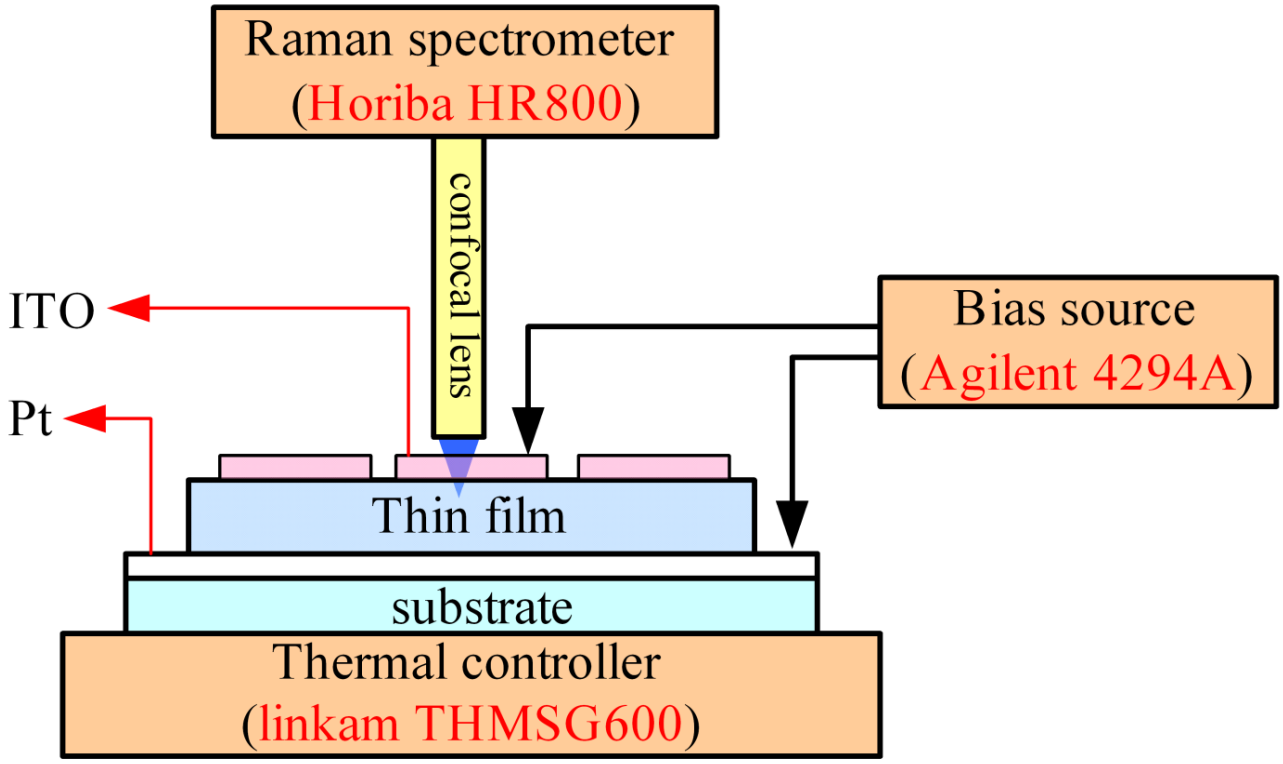

Figure S15. Schematic diagram for Raman scattering spectra as a function of an applied dc bias electric field of the thin film. The Agilent 4294 and the linkam THMSG600 were employed as a bias source and thermal controller, respectively. The ITO was deposited as a top electrode.

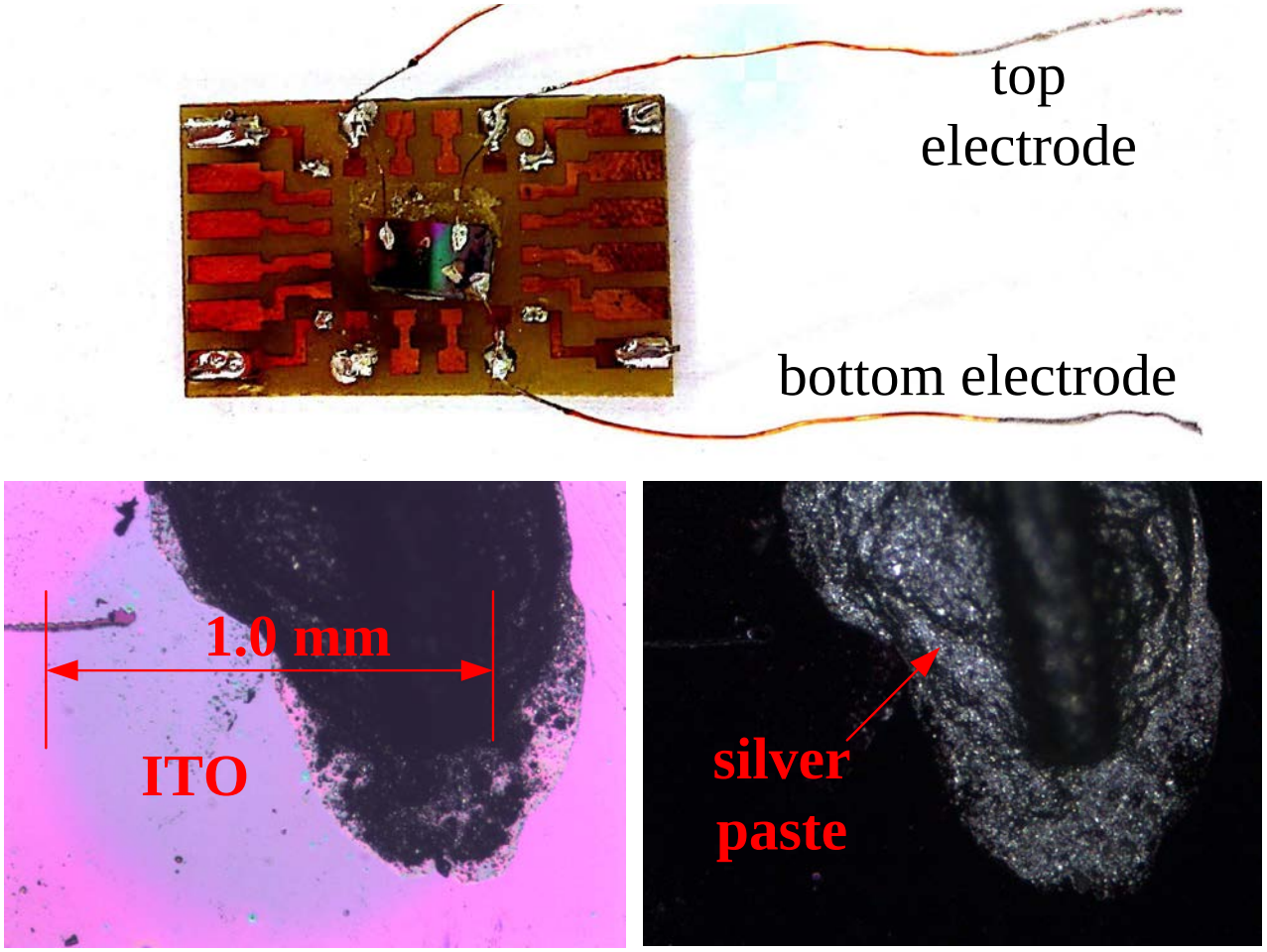

Figure S16. Prototype schematic diagram for Raman scattering spectra experiment of the BCT-BMT thin film under dc bias electric field. (a) Sample bridged by silver paste rather than by the wire bonding method to minimize damage. Optical microscope images of the ITO top electrode under bright field (b) and dark field (c).

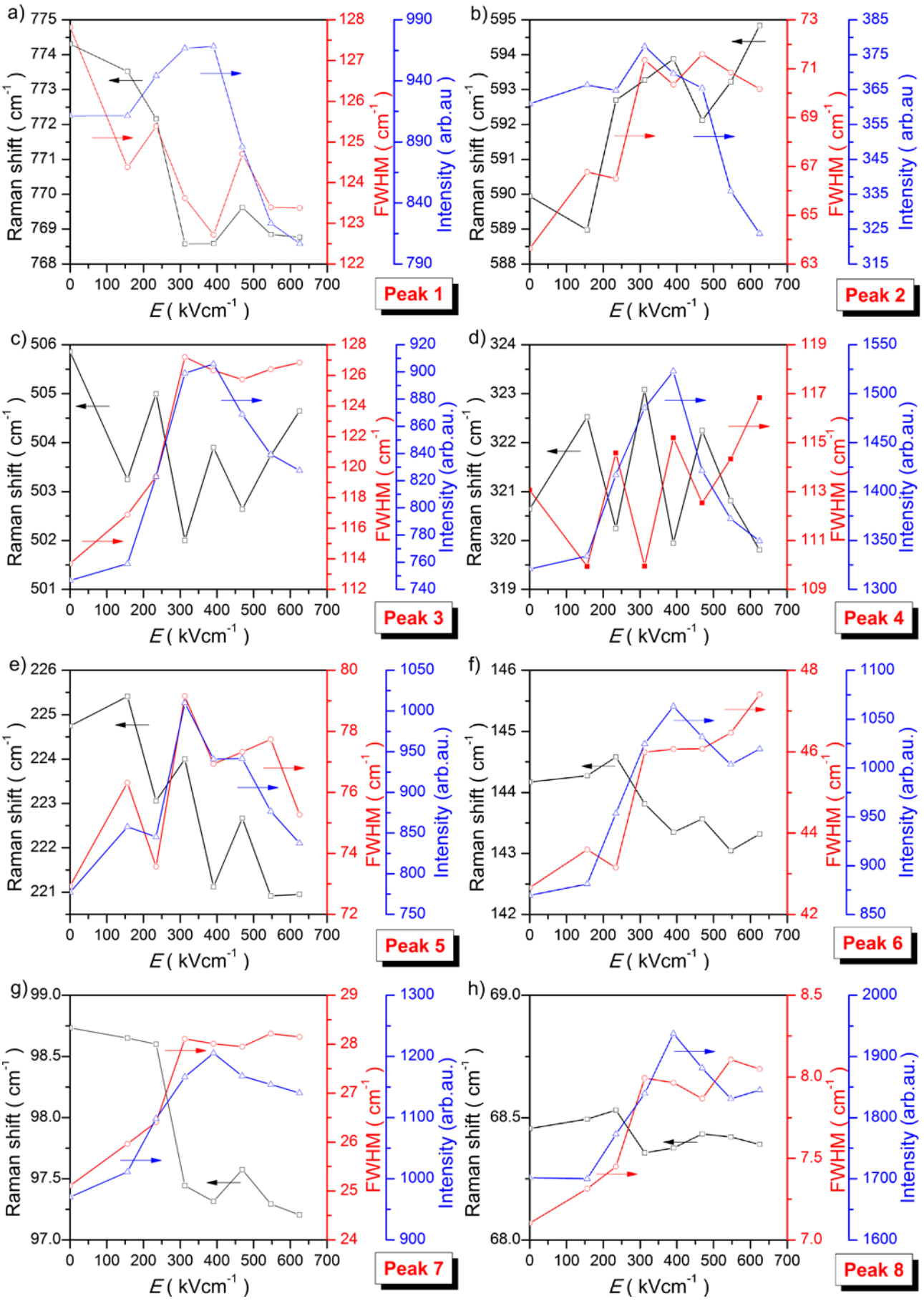
a)
Raman shift (cm-1)
FWHM (cm-1)
Intensity (arb.au)
E (kVcm-1)
Peak 1
b)
Peak 2
c)
Intensity (arb.au.)
Peak 3
d)
Peak 4
e)
Peak 5
f)
Peak 6
g)
Peak 7
h)
Peak 8

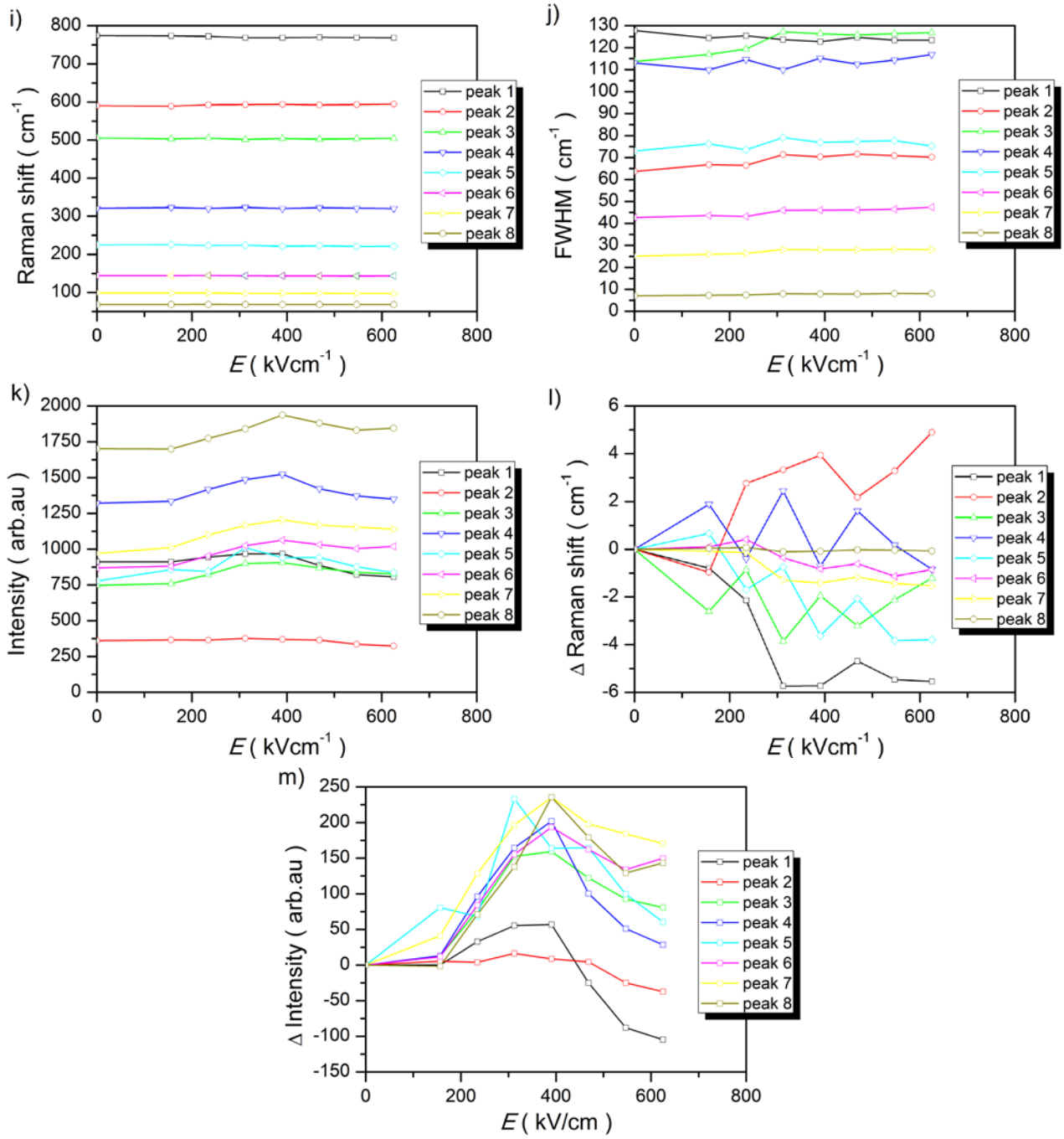

Figure S17. Raman scattering spectra measurements as a function of applied electric field of the BCT-BMT thin film. (a)-(h) Raman shift, FWHM and intensity for peaks 1-8, respectively. **i)** Raman shift, **j)** FWHM, **k)** intensity, **l)** Δ Raman shift and **m)** Δ intensity for all the peaks.

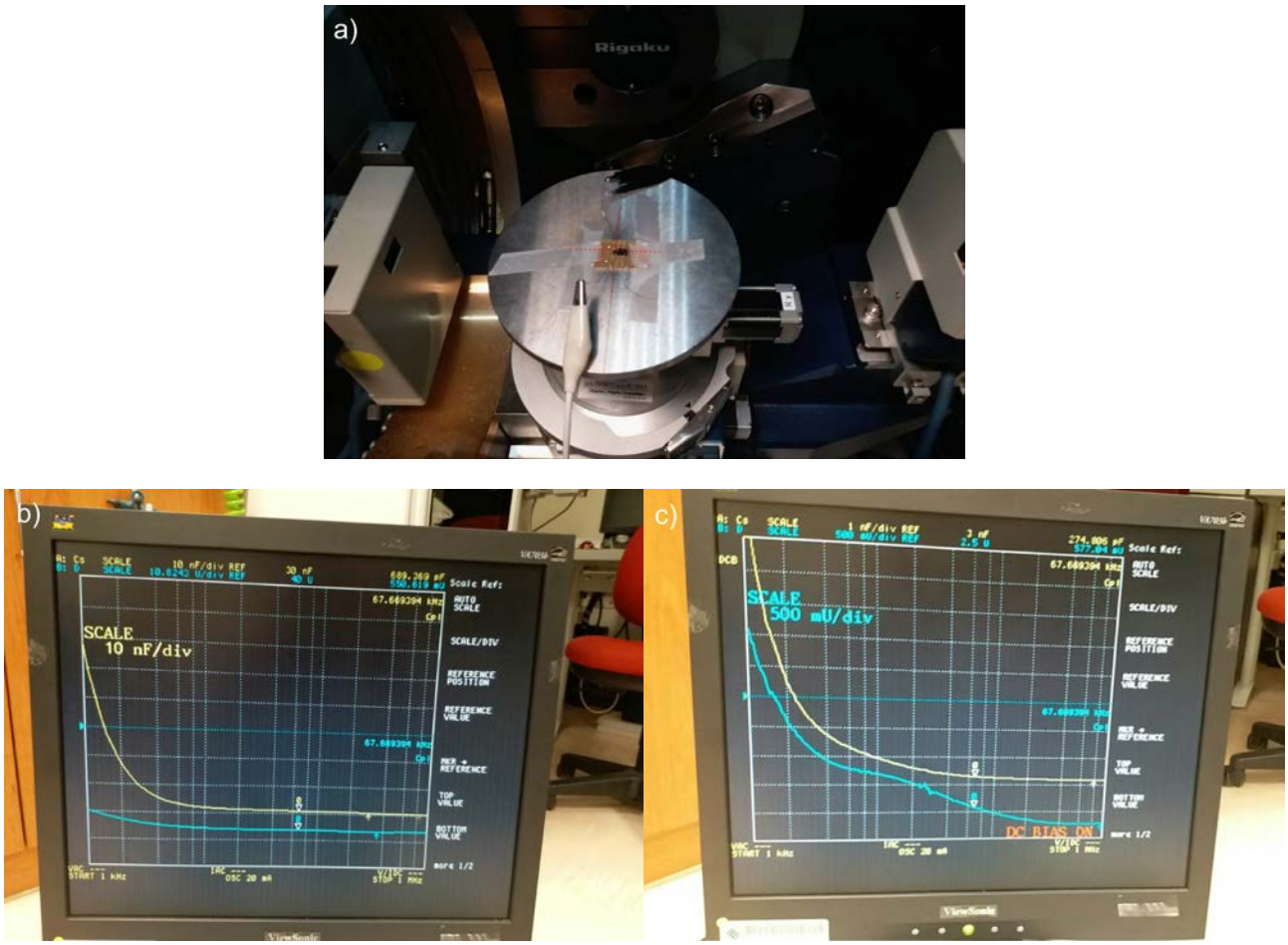

Figure S18. Photos for XRD patterns experiment of the BCT-BMT thin film under dc bias electric field using the Agilent 4294 as the dc bias source. (a) ITO top electrodes positioned by cross positioning method precisely. (b) And (c) Dc bias off and on, respectively.

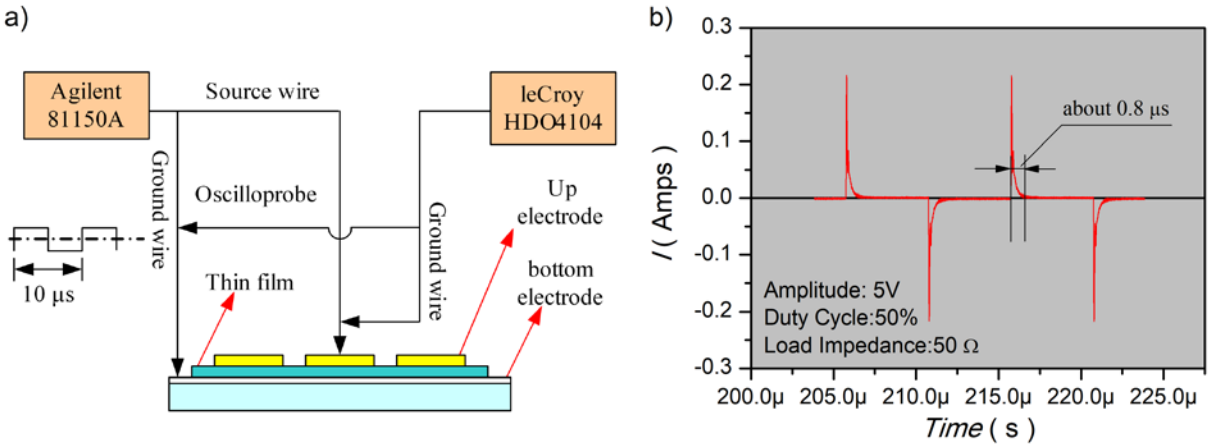

Figure S19. Power density measurements of the BCT-BMT thin film capacitor. (a) Schematic diagram for charge/discharge experiment of the thin capacitor. The Agilent 81150A was employed as a versatile signal source, and the leCroy HDO4104 was used as a digital oscilloprobe. The injected pulse voltage, duty cycle and the load impedance are set to 5 V, 50% and 50 Ω, respectively. **(b)** Charging/discharging current & time diagram. The charging/discharging time can be estimated to be about 0.8 μs.

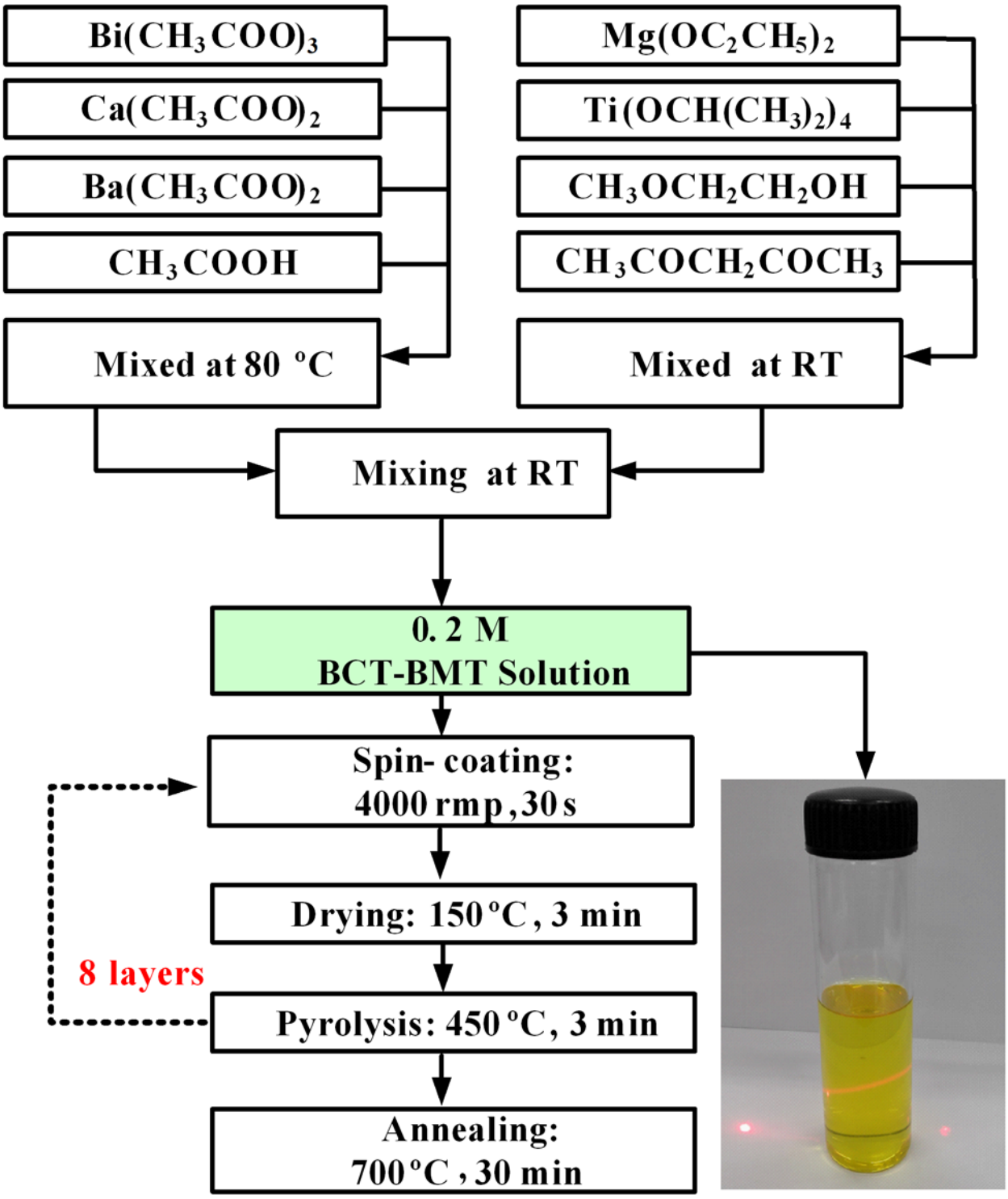

Figure S20. Flow chart of the sol-gel preparation and spin coating process for the $0.5(Ba_{0.8}Ca_{0.2})TiO_3$-$0.5Bi(Mg_{0.5}Ti_{0.5})O_3$ (BCT-BMT) thin film. The bright red light path inside the sol-gel of the bottle (the lower right corner) shows a typical Tyndall effect, indicating a good stability of the colloid system.

Table S1. Values of parameters A_{in} and A_{out} of some perovskite prototypical ferroelectric thin films.

Formula	(001)-oriented		(111)-oriented	
	A_{in} (10^4 K)	A_{out} (10^4 K)	A_{in} (10^4 K)	A_{out} (10^4 K)
$BaTiO_3$[2]	3.6	-4.7	3.1	-2.0
$PbTiO_3$[2]	3.5	-2.9	4.1	-1.8
$PbTiO_3$(I)[1]	8.6	-4.4	7.8	0.1
$PbTiO_3$(II)[1]	5.4	-4.5	5.5	-2.9
$PbTiO_3$(III)[1]	10.1	-4.7	16.3	1.1
0.7PMN-0.3PT[3]	5.7	-8.1	-1.6	1.4

Reference

1. Mtebwa M, Tagantsev AK, Yamada T, Gemeiner P, Dkhil B, Setter N. Single-domain (110)$PbTiO_3$ thin films: Thermodynamic theory and experiments. *Physical Review B* 2016, **93**(14).
2. Pertsev NA, Zembilgotov AG, Tagantsev AK. Effect of mechanical boundary conditions on phase diagrams of epitaxial ferroelectric thin films. *Phys Rev Lett* 1998, **80**(9)**:** 1988-1991.
3. Zhang H, Lu X, Wang R, Wang C, Zheng L, Liu Z, *et al.* Phase coexistence and Landau expansion parameters for a 0.70$Pb(Mg_{1/3}Nb_{2/3})O_3$−0.30$PbTiO_3$ single crystal. *Physical Review B* 2017, **96**(5).